A Layered Oxycarbonate Involving Trivalent Chromium: $Sr_4FeCrO_6CO_3$

Y. Bréard, C. Michel,* M. Hervieu, A. Ducouret, N. Nguyen, F. Studer, A. Maignan, and B. Raveau

Laboratoire CRISMAT, ISMRA, UMR-CNRS 6508, 6, Boulevard du Maréchal Juin, F14050 Caen Cédex, France

E. Suard

Institut Laue-Langevin, 6 rue Jules Horowitz, BP156, F38042 Grenoble Cedex 9, France

Received January 3, 2001. Revised Manuscript Received April 11, 2001

The possibility to synthesize layered oxycarbonates involving trivalent chromium has been shown for the first time for the compound $Sr_4Fe_{2-x}Cr_xO_6CO_3$, with $0 \le x \le 1$. The structural study of $Sr_4FeCrO_6CO_3$ using NPD, HREM, Mössbauer, and XANES, shows that this phase, which is closely related to n = three-member of the Ruddlesden−Popper family, is built up of layers of corner-sharing CrO_6 octahedra and FeO_5 pyramids. Between the layers the triangular CO_3 groups, parallel to *bc* or *ac* planes, are connected to the CrO_6 octahedra, adopting a "coat-hanger" configuration. The antiferromagnetic behavior of this phase (T_N = 125 K) is fundamentally different from the magnetic behavior of $Sr_4Fe_2O_6CO_3$.

Introduction

The discovery of superconductivity in layered cuprates (see ref 1 for a review) and of colossal magnetoresistance in layered manganites[2] has shown that all these oxides, which derive from the Ruddlesden−Popper (RP) family,[3] are of high potential for a new physics. Such structures, which consist of intergrowths of rock salt type layers with perovskite layers, can themselves be intergrown with oxycarbonates, as was shown in the case of copper oxycarbonate supercondutors.[1]

In contrast to copper, very few transition elements can accommodate carbonate layers. Recent investigations of iron-based systems have shown the ability of Fe^{3+} to form layered oxycarbonates $Sr_4Fe_{3-x}O_{10-4x-\delta}(CO_3)_x$,[4,5] whose structure derives from the RP-type phase $Sr_4Fe_3O_{10}$[6] by replacing totally or partly the FeO_6 octahedra of the middle layer by carbonate groups. In this paper, we show the ability of trivalent chromium to accommodate such oxycarbonate layered structures, forming the solid solution $Sr_4Fe_{2-x}Cr_xO_6CO_3$, with $0 \le x \le 1$. The detailed structural study of $Sr_4FeCrO_6CO_3$ demonstrates that Cr^{3+} and Fe^{3+} adopt an octahedral and a pyramidal coordination, respectively, and that the CO_3 groups are linked to the CrO_6 octahedra and exhibit an original "coat-hanger" configuration. The antiferromagnetic behavior of this phase, being very different from that of the pure iron compound $Sr_4Fe_2O_6CO_3$,[4] is also evidenced.

Experimental Section

Synthesis. The different oxides with composition $Sr_4Fe_{2-x}Cr_xO_6CO_3$ have been prepared from appropriate mixtures of Fe_2O_3, Cr_2O_3, SrO, and $SrCO_3$, which was used as CO_2 source. The compounds were intimately mixed, pressed in the form of bars, introduced in evacuated silica tubes, and heated to 1200 °C for 12 h. Heating and cooling to room temperature were performed in 6 h. For the neutron diffraction study, approximately 5 g of $Sr_4FeCrO_6CO_3$ was prepared according to the same procedure.

Iron and Chromium Oxidation States. The oxidation states of chromium and iron were determined by chemical analysis, using redox back-titration. Powder was dissolved in a mixture of 2 N hydrochloric acid and 1 N orthophosphorous acid containing a known amount of $FeCl_2$ solution. Fe^{2+} ions are oxidized to Fe^{3+} by iron and chromium ions, in higher oxidation states, contained in the sample, and then the remaining Fe^{2+} are titrated by potassium dichromate. Both elements where found to be trivalent, in agreement with Mössbauer data and neutron diffraction results, confirming for $x = 1$ the formula $Sr_4FeCrO_6CO_3$.

Structural Analysis. The electron diffraction (ED) investigation was carried out with a JEOL 200CX microscope, tilting around the crystallographic axes. The high-resolution electron microscopy (HREM) study was performed with a TOPCON 002B, operating at 200 kV and having a point resolution of 1.8 Å. Image calculations were carried out using the Mac Tempas program. Both microscopes are equipped with an EDX analyzer.

Phase purity was checked by X-ray diffraction using a PHILIPS vertical diffractometer PW1370 equipped with a graphite secondary monochromator and working with the Cu Kα radiation. Data were collected by step scanning of 0.025° (2θ) over an angular range $5° < 2\theta < 120°$. X-ray diffraction patterns were used for lattice constant measurements.

(1) Rao, C. N. R.; Raveau, B. In *Transition Metal Oxides*; Wiley-V.C.H.: New York, 1998. Raveau, B.; Michel, C.; Hervieu, M.; Groult, D. In *Crystal Chemistry of High-Tc Superconducting Oxides*; Springer-Verlag: New York, 1991.

(2) Moritomo, Y.; Asamitsu, A.; Kuwhara, H.; Tokura Y. *Nature* **1996**, *380*, 141.

(3) Ruddlesden, S. R.; Popper, P. *Acta Crystallogr.* **1957**, *10*, 538; **1958**, 11, 54.

(4) Yamaura, K.; Huang, O.; Lynn, J. W. ; Erwin, R. W.; Cava, R. J. *J. Solid State Chem.* **2000**, *152*, 374.

(5) Bréard, Y.; Michel, C.; Hervieu, M.; Raveau, B. *J. Mater. Chem.* **2000**, *10*, 1043.

(6) Brisi, C.; Rolando, P. *Ann. Chim.* (Roma) **1969**, *59*, 385.

10.1021/cm010004i CCC: $20.00 © 2001 American Chemical Society
Published on Web 06/26/2001

Neutron powder diffraction data were collected at room temperature at ILL (Grenoble, France) on the high-resolution D2B diffractometer, using the wavelength 2.398 Å, in the angular range $0° < 2\theta < 162.5°$ with steps of 0.05° (2θ). The scattering lengths of the different atoms were those included in the Rietveld profile analysis program package (FULL-PROF[7]).

X-ray Absorption Spectroscopy. The X-ray absorption spectra at Cr and Fe K-edges were recorded at room temperature in a classical transmission mode at the EXAFS I station (channel cut monochromator) using the synchrotron radiation of the DCI storage ring of LURE (Orsay, France) working at 1.85 GeV with a 250 mA current. The energy resolution at the Cr K-edge is estimated at 5989 eV, whereas it is estimated at 7112 eV for the Fe K-edge. The normalization procedure used throughout this work was a standard one: after subtraction of the same diffusion background on the XANES and EXAFS spectra, recorded under the same experimental conditions, a point located at an energy of 800 eV from the edge, where no more EXAFS oscillations were observable, was set to unity. Then the intensity of a point with an energy betwen 50 and 100 eV from the edge was recorded on the EXAFS spectrum and reported on the XANES to set the normalization height.

Magnetism and Mössbauer Spectroscopy. Magnetic susceptibility $\chi(T)$ measurements were investigated in the range 5−400 K using an AC-DC SQUID Quantum Design magnetometer (ZFCW−FCW method) with an applied field of 3 kG. For high-temperature measurements ($300 \text{ K} < T < 800$ K), data were collected with the Faraday method using a Cahn RG microbalance.

The ^{57}Fe Mössbauer spectrum at room temperature of the powdered $Sr_4Fe_2CrO_6CO_3$ sample was recorded using a conventional spectrometer operating in the constant acceleration mode. ^{57}Co/Rh was used as the γ-ray source. The isomer shift (IS) is referred to metallic iron.

Results and Discussion

The solid solution, $Sr_4Fe_{2-x}Cr_xO_6CO_3$, was studied for $0 < x < 2$. After thermal treatment, products appeared as black sintered bars. All samples were monophasic for $x \leq 1$, if one excepts $SrCO_3$, which is sometimes observed in a very small quantity on the X-ray powder diffaction patterns (Figure 1). The XR powder diffraction data are very close to those of $Sr_4Fe_2O_6CO_3$[4] and $Sr_4Fe_{2.6}O_{8.2}(CO_3)_{0.4}$[5] and can be indexed in a tetragonal cell (space group $I4/mmm$) with cell parameters $a \approx a_p \approx 3.9$ Å and $c \approx 28$ Å. The variation of the lattice constants as a function of the chromium substitution rate, x, is plotted in Figure 2. One can see a very small and continuous increase of a when x increases, whereas c decreases with higher extent. The decrease of c is higher than that expected from the partial replacement of Fe^{3+} by Cr^{3+} (valence states assumed from oxygen stoichiometry and confirmed by Mössbauer and XANES) and could be due to small changes in some atomic arrangements.

Electron Microscopy Study. The $Sr_4FeCrO_6CO_3$ sample prepared for the ND study was characterized by ED, HREM, and EDS. Reconstructing the reciprocal space by tilting around the crystallographic axes confirms the cell parameters and shows that the majority of the crystallites exhibit reflection conditions consistent with the $I4/mmm$ space group. Typical [001] and [100] ED patterns are given in Figure 3a and b. In the other crystallites, very weak and often diffuse extra spots show that the I-type symmetry is violated.

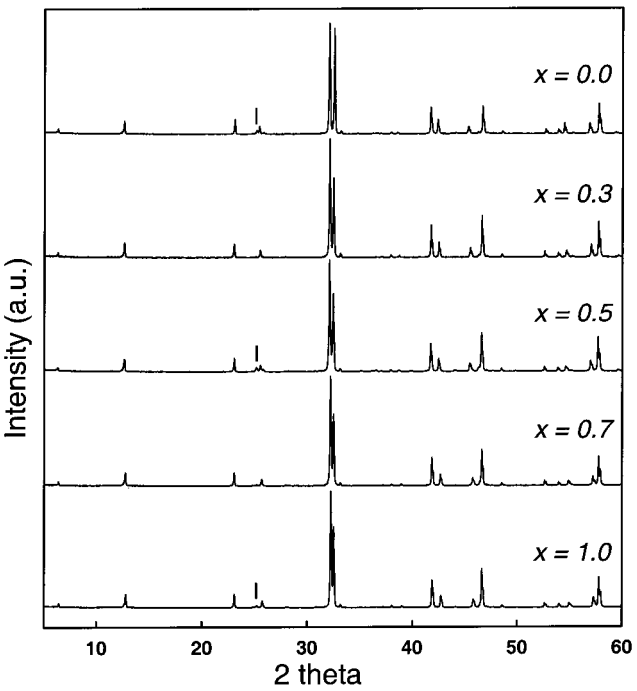

Figure 1. X-ray powder diffraction pattern of some compositions of the solid solution $Sr_4Fe_{2-x}Cr_xO_6CO_3$. For $x = 0.0$, 0.5, and 1.0, the main diffraction peak of $SrCO_3$ (stick) is observed.

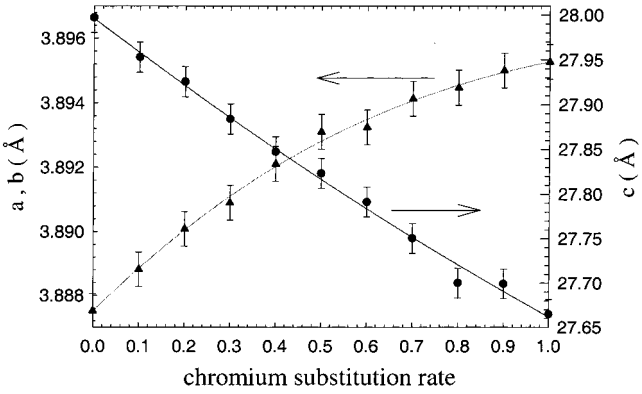

Figure 2. Evolution of the lattice constants as a function of the chromium substitution rate for $Sr_4Fe_{2-x}Cr_xO_6CO_3$.

The nature and the stacking mode of the different layers are easily visible by viewing the crystals along [100]. This is illustrated in the [100] HREM image displayed in Figure 4; it is recorded for a focus value close to −25 nm; i.e., the bright dots are correlated to the light electron density zones. The experimental contrast fits with the theoretical one calculated for a crystal thickness of 24 Å and a focus value of −25 nm, using the refined position parameters (see next section) as shown in the inset. However, the HREM investigation shows that there frequently exist local deviations of the experimental contrast, with regard to the "ideal" calculated one. These defects sometimes run over a few nanometers long but are never periodically established, even over a short range distance. The experimental focus series shows that the carbonate rows as well as the Fe/Cr rows are locally defective. In the course of the system investigation, we observed that the appearance frequency and extent of these areas strongly depend on

(7) Rodriguez Carvajal, J. *Collected Abstract of the Satellite Meeting on Powder Diffraction of the XVth Congress of the International Union of Crystallography*, Toulouse, France, 1990, p 127.

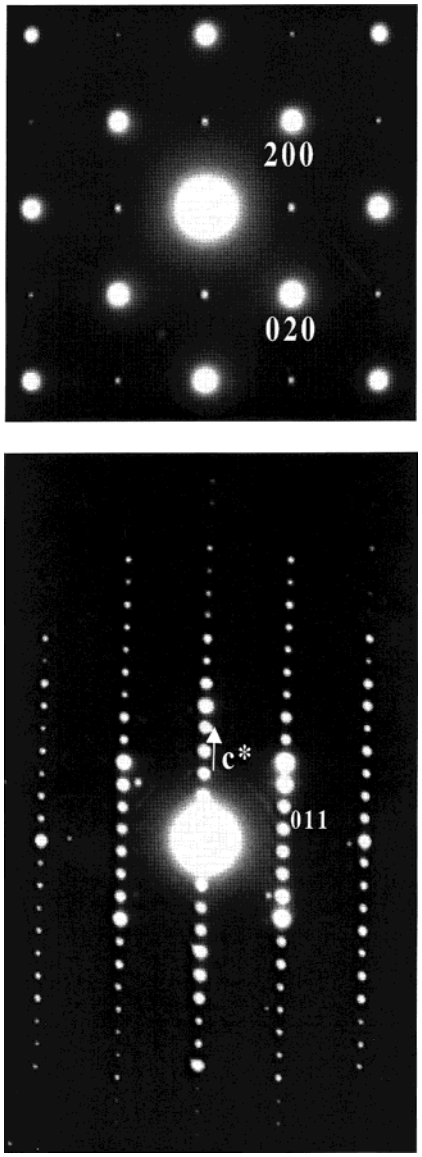

Figure 3. (a) [001] and (b) [100] ED pattern of $Sr_4FeCrO_6CO_3$.

the nominal composition and thermal process. Moreover, they are clearly correlated to the extra reflections that violate the *I*4/*mmm* symmetry. A detailed TEM analysis of these phenomena is in progress.

Neutron Diffraction Study. Calculations were carried out in the space group *I*4/*mmm*, which implies the absence of order between the chromium and iron atoms. $SrCO_3$ was introduced as the secondary phase.

Bearing in mind the structures previously described for the oxycarbonates $Sr_2CuO_2CO_3$[8,10] and $Tl_{0.5}Pb_{0.5}Sr_4Cu_2CO_3O_7$[9], the starting structural model of $Sr_4FeCrO_6CO_3$ (Figure 5a) was considered to be an intergrowth of $Sr_2(Fe,Cr)_1O_2CO_3$ layers and $Sr_2(Fe,Cr)_1O_4$ layers. The results obtained for this structural model were not satisfactory and suggested the possibility of a different configuration of the carbonate layers. Thus in a first step the CO_3 groups were omitted, and Fourier

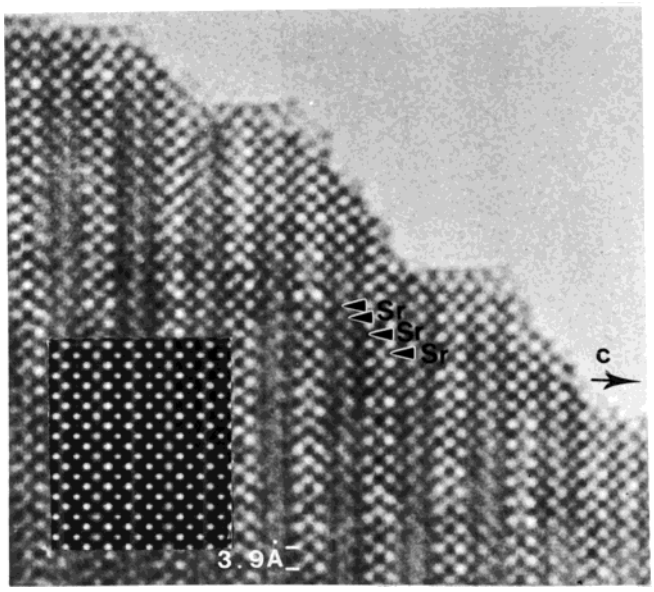

Figure 4. [100] HREM of $Sr_4FeCrO_6CO_3$. The bright dots are correlated to the light electron density zones. The Sr positions are indicated by black arrows, and the calculated image is superposed on the experimental one.

difference sections at the level of those groups clearly showed three positive residues at 0,0,0 (2a site) and at 0,0,±0.06 (4e site) (Figure 6a) that could be attributed to carbon and O(3) oxygen, respectively. The introduction of these atoms allowed the Bragg factor to decrease from 27% to 16%. New Fourier difference maps (Figure 6b) evidenced positive residues at a new site (O(4)) with coordinates ±0.3,0,0. The partial occupation of this site by oxygen, in the proportion of one oxygen atom per carbon, allowed the Bragg *R* factor to be decreased to $R_B = 7.1\%$. At this stage the results led to a model close to the starting one. Nevertheless, the extremely high thermal factor of O(3) ($B = 12.8$ Å^2) and the residues observed at the level of the position suggested both a partial site occupancy and/or a possible displacement of O(3) from its position. Moreover, a new map section at the level of O(4) positions showed the presence of small residues at ±0.3,0,±0.02, indicating a possible displacement along $\vec{c}$. Taking into consideration these observations, the O(4) atoms were distributed over the 16n sites; positional parameters and site occupancy were successively refined for these two oxygen atoms, leading to a significant improvement of the fit ($R_B = 5.3\%$) for occupancy factors close to 50% and 25% for O(3) and O(4), respectively. Final refinements were then carried out by fixing the number of oxygen atoms in the O(3) and O(4) sites (n O(3) = n C and n O(4) = 2n C), including for these atoms anisotropic thermal vibrations and delocalizing carbon over the 4e sites. The fit converged to $R_p = 4.7\%$, $R_{wp} = 6.4\%$, and $R_B = 4.1\%$ with the refined atomic parameters listed in Table 1. The calculated NPD pattern is in agreement with the experimental one (Figure 7).

All structural refinements of oxycarbonates have shown that the exact configuration of the CO_3 groups in the structure is not easy to establish, even with neutron diffraction data,[4,10−13] due to disorder of the

(8) Greaves, C.; Slater, P. R. *Physica C* **1991**, *175*, 172.
(9) Huvé, M.; Michel, C.; Maignan A.; Hervieu, M.: Martin C.; Raveau, B.; *Physica C* **1993**, *205*, 219.
(10) Babu, T. G. N.; Fisch, D. J.; Greaves, C. *J. Mater. Chem.* **1991**, *1*, 677.
(11) Miyazaki, Y.; Yamane, H.; Kajitani, T.; Oku T.; Hiraga K.; Morii Y.; Fuchizaki F.; Funahashi S.; Hirai T. *Physica C* **1992**, *1*, 434.

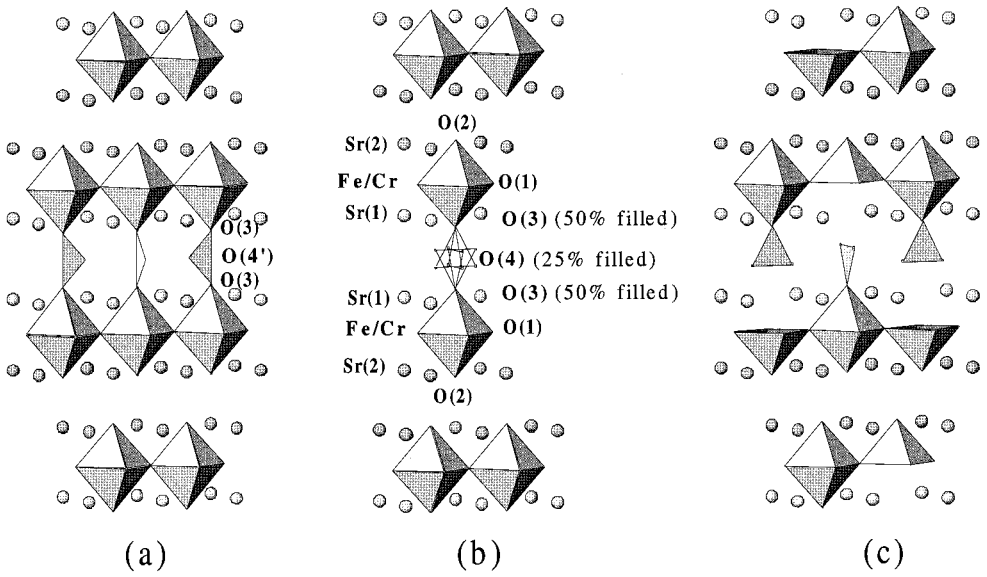

Figure 5. (a) Starting structural model for $Sr_4FeCrO_6CO_3$ structure determination, based on the intergrowth of $Sr_2(Fe,Cr)_1O_2$-CO_3 and $Sr_2(Fe,Cr)_1O_4$ layers. (b) Distribution and positions of oxygen at the level of the carbonate groups in the actual structure deduced from NPD data. (c) Schematic view of the structure of $Sr_4FeCrO_6CO_3$ showing the "coat-hanger" configuration of the triangular CO_3 groups linked to the CrO_6 octahedra, iron being in pyramidal coordination. The orientation of the carbonate groups is given as an example.

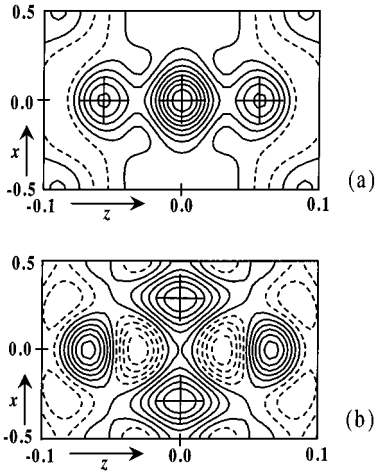

Figure 6. Difference Fourier map section at $y = 0$ calculated at different stages of the refinement (see the text): (a) positive residues attributed to C and O(3), (b) negative and positive residues at the level of O(3) positions and positive residues attributed to O(4). For each map the scale in the third direction is different, so the size of the residues cannot be compared.

oxygen atoms surrounding the carbon. This disorder consists of a delocalization over more general positions with partial occupancies, leading for neighboring atoms to different local environments that depend on the oxygen position and its occupancy. In our case the disordering is also imaged by anisotropic thermal displacements (Table 1), which are important in the *ab* plane for O(3) and in the *ac* plane for O(4). They probably are the result of small vibrational displacements around the refined positions. It should be noted that calculations with more general positions and isotropic *B* factors for these two atoms damage the fit.

Table 1. Refined Crystal Parameters Obtained from NPD Data for $Sr_4FeCrO_6CO_3$[a]

atom	site	*x*	*y*	*z*	U_{iso} (Å^2)	*n*
Sr(1)	4e	0.0	0.0	0.5725(2)	0.004(1)	4
Sr(2)	4e	0.0	0.0	0.7003(2)	0.006 (2)	4
Fe/Cr	4e	0.0	0.0	0.1435(2)	0.001(2)	2/2
C	4e	0.0	0.0	0.009 (1)	0.000(4)	2
O(1)	8g	0.0	0.5	0.6316 (2)	0.006 (1)	8
O(2)	4e	0.0	0.0	0.2104(2)	0.010(2)	4
O(3)	4e	0.0	0.0	0.0546(3)	*b*	2
O(4)	16*n*	0.269(5)	0.0	0.015(1)	*b*	4

[a] Space group $I4/mmm$, $a = 3.89477(8)$ Å, $c = 27.6961(8)$ Å; $R_p = 4.7\%$, $R_{wp} = 6.4\%$, and $R_B = 4.1\%$; 2 wt % impurity. [b] O(3), $U_{11} = U_{22} = 0.041(9)$, $U_{33} = 0.013(20)$, $U_{12} = U_{13} = U_{23} = 0$; O(4), $U_{11} = 0.107(15)$, $U_{22} = 0.031(4)$, $U_{33} = 0.108(46)$, $U_{13} = -0.099(30)$, $U_{12} = U_{23} = 0$.

The present refinements show that the structure of $Sr_4FeCrO_6CO_3$ (Figure 5b), although closely related to that of starting structural model (Figure 5a), is significantly different at the level of the carbonate layers. The O(3) sites that were fully occupied in the starting model are half-occupied in $Sr_4FeCrO_6CO_3$, so half of the transition metal polyhedra are octahedra and half are tetragonal pyramids distributed randomly. In contrast to O′(4) sites of the structural starting model (Figure 5a), the oxygen atoms in the O(4) sites (Figure 5b) are twice as numerous, so the CO_3 groups exhibit a "coat-hanger" configuration (Figure 5c) instead of "flaglike" configuration in the model (Figure 5a). Such a configuration is similar to that observed for the BO_3 goups in $LaBaCuO_2BO_3$[14] and corresponds to one of the possible configurations proposed for $Sr_4Fe_2O_6CO_3$.[4] The triangular CO_3 groups are parallel to the *ac* or *bc* planes, where they can accommodate two different orientations (Figure 8a). They can be distributed at random in the structure in connection with the random distribution of the octahedra and tetragonal pyramids. Bearing in mind that Cr^{3+} adopts generally the octahedral coordi-

(12) Chaillout, C.; Huang, Q.; Cava, R. J.; Chenavas, J.; Santoro, A.; Bordet, P.; Hodeau, J. L.; Krajewski, J. J.; Levy, J. O.; Marezio, M.; Peck, W. F., Jr. *Physica C* **1992**, *195*, 335.

(13) Malo, S.; Michel, C.; Pelloquin, D.; Hervieu, M.; Toulemonde, O.; Raveau, B. *Physica C* **1998**, *304*, 213.

(14) Norrestam, R.; Kritikos, M.; Sjodin, A. *Acta Crystallogr. B* **1994**, *50*, 631.

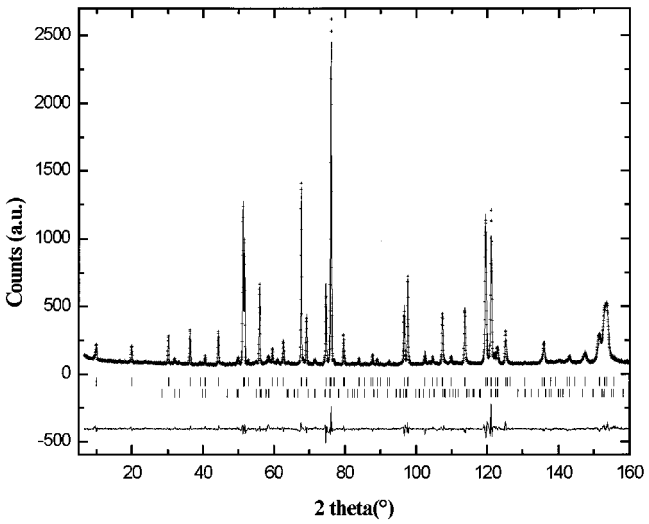

Figure 7. Experimental (crosses), calculated, and difference (solid lines) neutron powder diffraction pattern of $Sr_4FeCrO_6CO_3$ at the end of refinement. The vertical bars are the Bragg positions for the main phase (upper) and the impurity (lower).

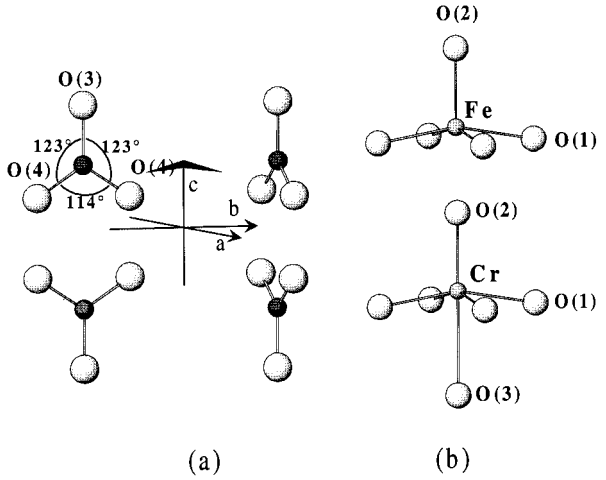

Figure 8. (a) Geometry of the CO_3 group and possible different orientations with regard to the crystallographic axes and (b) proposed geometry for chromium and iron polyhedra.

nation and that Fe^{3+} is able to accommodate both octahedral and pyramidal coordinations, it is most likely that the structure of $Sr_4FeCrO_6CO_3$ consists of CrO_6 octahedra connected to CO_3 groups and FeO_5 tetragonal pyramids (Figure 8b). Such a model explains why the solid solution $Sr_4Fe_{2-x}Cr_xO_6CO_3$ cannot be obtained for $x > 1$, due to the inability of Cr^{3+} to adopt the pyramidal coordination. The pyramidal coordination of Fe^{3+} in $Sr_4FeCrO_6CO_3$ is demonstrated further by comparison between Mössbauer spectroscopy and EFG calculations. The selected interatomic distances, compatible with the reasonable Fe−O, Cr−O, and C−O distances (Table 2), show that the triangular groups are pratically regular with C−O bonds ranging from 1.23 to 1.25 Å and O−C−O angles ranging from 114 to 123°. Note that two successive CO_3 groups must be rotated by 90° to avoid too short O(4)−O(4) intercarbonate distances. The CrO_6 octahedra are distorted with four equatorial Cr−O bonds of 1.97 Å and an abnormally short apical bond (1.85 Å) opposed to a long one (2.46 Å). The FeO_5 pyramid is compressed with four identical equatorial bonds (1.97 Å) and one short apical bond (1.85 Å).

Table 2. Selected Interatomic Distances and Angles

bond	bond distances (Å)	×*n*	bond	bond distances (Å)	×*n*
Sr(1)−O(3)	2.798(4)	4	Fe/Cr−O(3)	2.46(2)	0.5
Sr(1)−O(1)	2.544(4)	4	Fe/Cr−O(2)	1.854(8)	1
Sr(1)−O(4)	2.68(2)		Fe/Cr−O(1)	1.975(2)	4
Sr(2)−O(2)	2.474(8)	1	C−O(3)	1.25(4)	1
Sr(2)−O(2)	2.768(2)	4	C−O(4)	1.24(4)	2
Sr(2)−O(1)	2.722(4)	4			
bond	bond angle (deg)	×*n*	bond	bond angle (deg)	×*n*
O(3)−C−O(4)	123(1)	2	O(4)−C−O(4)	114(2)	1

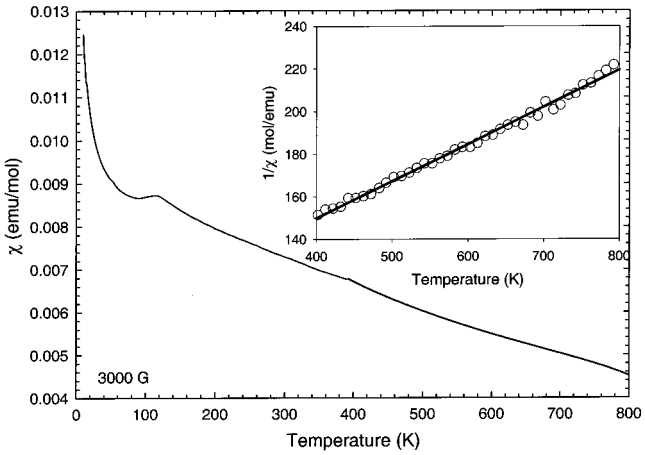

Figure 9. $\chi_M(T)$ curve obtained from the ZFC $M(T)$ curve recorded at 3000 G. Inset: $\chi_M^{-1}(T)$ curve (open circles are the experimental points, whereas the solid line is the fit).

Magnetism. The magnetic susceptibility measurements performed in the range 5−800 K, in an applied magnetic field of 3000 G, for $Sr_4FeCrO_6CO_3$ show an antiferromagnetic transition at $T_N = 125$ K (Figure 9). The linear part of χ_M^{-1} (inset Figure 9) was fitted with the Curie−Weiss law $\chi = \chi_0 + C/(T - \theta p)$ (C is the Curie constant, θp is the paramagnetic Curie temperature, and χ_0 is the temperature independent susceptibility). The important negative θp value (−460 K) is characteristic of strong antiferromagnetic interactions in this compound. From the Curie constant, an effective magnetic moment value (μ_{eff}) of 6.8 μ_B is obtained. This value is close to the expected one calculated by considering Fe^{3+} and Cr^{3+} in the high-spin configuration ($\mu_{calc} = 7.07$ μ_B). This behavior is very different than that observed for the chromium-free oxycarbonate $Sr_4Fe_2O_6CO_3$, which exhibits a three dimensional magnetic ordering transition at 361 K characterized by an antiferromagnetic order within the $FeO_2/SrO/SrO/FeO_2$ blocks and a ferromagnetic order between the blocks.[4] It has been predicted by Goodenough[15] that the superexchange bewteen a d^3 ion and a d^5 ion will be ferromagnetic if the bond angle at the intervening anion is sufficiently close to 180°. In the case of $Sr_4FeCrO_6CO_3$ (the bond angle is closed to 161°) we have not observed such coupling between Fe and Cr ; on the contrary, the Cr^{3+} ($3d^3$) for Fe^{3+} ($3d^5$) substitution tends to suppress the ferromagnetic interactions that exist in the Cr-free $Sr_4Fe_2O_6CO_3$ oxycarbonate. A systematic study of the compounds $Sr_4Fe_{2-x}Cr_xO_6CO_3$, using neutron diffrac-

(15) Goodenough, J. B. *Magnetism and the chemical Bond;* Interscience: New York, 1963.

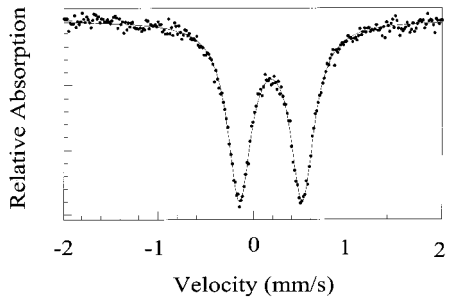

Figure 10. Mössbauer spectrum of $Sr_4FeCrO_6CO_3$ reported at room temperature.

tion, will be necessary to understand the magnetic structure of these compounds.

Mössbauer Spectroscopy and Electric Field Gradient Calculations. To check the above hypothesis about the pyramidal coordination for iron, the Mössbauer spectrum of $Sr_4FeCrO_6CO_3$ was registered at room temperature. The spectrum (Figure 10) shows the existence of pure quadrupolar electric interactions at 293 K. One iron site is evidenced by the fit; its IS value (0.29 ± 0.02 mm/s) corresponds to a trivalent charge. The quadrupole splitting (QS = 0.66 ± 0.02 mm/s) of the paramagnetic doublet results from the interaction between the Fe^{3+} nucleus and the surrounding ions of the structure.

To determine the local symmetry of the iron site, electric field gradient (EFG) calculations have been performed in several oxygen surroundings (octahedral or pyramidal) and various cationic environments (iron and chromium). Calculations of the EFG tensor $[V_{ij}]$ have been limited to the monopolar part of the potential development in a crystal field model. These calculations only include the "lattice contribution" to the $[V_{ij}]$ tensor at the iron nucleus; the "valence contribution" is vanishing because the spherical symmetry of the $3d^5$ electronic orbital of Fe^{3+}.

Calculations in the whole crystal can only lead to a mean value between neighboring situations of octahedral and pyramidal oxygen first environments, owing to the partial occupancy of some crystallographic sites due to the disorder of C, O(3), and O(4). So we preferred "cluster" calculations including only ions in the range $d_{Fe-ligand} \leq 5$ Å, with atomic positions determined by the structural study.

The quadrupole splitting of the Mössbauer spectra can be calculated using

$$QS = \frac{eQ}{2}(1 - \gamma_\infty)V_{zz}\left(1 + \frac{\eta^2}{3}\right)^{1/2}$$

where $Q \approx 0.2$ barn is the quadrupolar moment of iron in the excited state, $(1 - \gamma_\infty) \approx 10.14$ is the Sternheimer antishelding factor for Fe^{3+}, V_{zz} is the principal component of the $[V_{ij}]$ EFG tensor, and $\eta = (V_{xx} - V_{yy})/V_{zz}$ is the asymmetry parameter.

Nine different cationic environments in the *ab* plane were considered (Figure 11); in both cases pyramidal and octahedral environments for Fe^{3+} and consequently octahedral and pyramidal environments for Cr^{3+} were examined. The results are given in Table 3. Compared with the experimental value, QS = 0.66(2) mm/s, and despite the crudeness of the approximation in the EFG calculations, the calculated values of the quadrupole

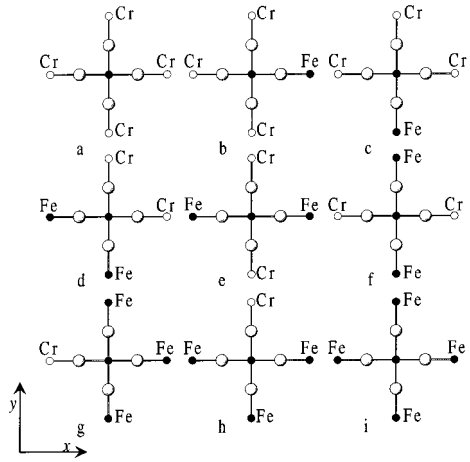

Figure 11. The nine possible environments of iron cation in the $(Fe_{0.5}Cr_{0.5})O_2$ plane.

Table 3. Room-Temperature EFG Calculations for Different in-Plane nearest Neighboring Cations of Fe^{3+} in Different Oxygen Environments

	cationic configurations[a]	probability (%)	pyramid calcd QS (mm/s)	pyramid η	octahedron calcd QS (mm/s)	octahedron η
a	$4Cr^{3+}$	6.25	0.78(1)	0.07(3)	0.16(1)	0.89(3)
b	$3Cr^{3+} + Fe^{3+}_{\|\|}$	12.50	0.78(1)	0.09(3)	0.18(1)	0.20(3)
c	$3Cr^{3+} + Fe^{3+}_{\perp}$	12.50	0.72(1)	0.16(3)	0.23(1)	0.92(3)
d	$2Fe^{3+} + 2Cr^{3+}$ cis	25.00	0.72(1)	0.18(3)	0.24(1)	0.13(3)
e	$2Fe^{3+}_{\|\|} + 2Cr^{3+}_{\perp}$	6.25	0.66(1)	0.27(3)	0.30(1)	0.93(3)
f	$2Fe^{3+}_{\perp} + 2Cr^{3+}_{\|\|}$	6.25	0.77(1)	0.28(3)	0.18(1)	0.89(3)
g	$3Fe^{3+} + Cr^{3+}_{\|\|}$	12.50	0.66(1)	0.07(3)	0.30(1)	0.32(3)
h	$3Fe^{3+} + Cr^{3+}_{\perp}$	12.50	0.71(1)	0.22(3)	0.23(1)	0.37(3)
i	$4Fe^{3+}$	6.25	0.64(1)	0.15(3)	0.28(1)	0.08(3)
	experimental		0.66(2)			

[a] || and ⊥ refer to the orientation of the CO_3 group, at the level of the central atom, assumed to be parallel to *ac*.

splitting show without ambiguity that the Fe^{3+} polyhedron is a pyramid in $Sr_4FeCrO_6CO_3$. It is not reasonable to choose one cationic configuration rather than another considering the dispersion of the QS values. Since no ordering between Fe^{3+} and Cr^{3+} is observed, all the configurations are possible with different probabilities. Considering a purely statistical distribution, the probability of each configuration (see Table 3) allows calculation of a weighted $[\bar{V}_{ij}]$ tensor that should correspond to the "macroscopic" situation. Under these conditions, the diagonalization of this $[\bar{V}_{ij}]$ tensor leads to a mean value $\overline{QS} = 0.71(1)$, which remains close to the experimental one, and a small asymmetry parameter $\bar{\eta} = 0.02(3)$.

Note that the same calculations with identical cationic environments in the *ab* plane but with a mean situation between the octahedral and pyramidal polyhedron would give $\overline{QS} = 0.46(1)$ and $\bar{\eta} \approx 0.08(3)$. These $\overline{QS}$ and $\bar{\eta}$ are close to the values obtained for the whole crystal (QS = 0.44(1) and $\eta = 0$) using partial occupancy for C, O(3), and O(4) sites. This is an indication that ions further than 5 Å from the central Fe^{3+} are quite negligeable in the monopolar EFG calculations and justifies the size of the "clusters" used above.

XANES Spectroscopy. To confirm the octahedral coordination of chromium, a XANES study of $Sr_4FeCrO_6CO_3$ was performed. The chromium K-edge of $Sr_4FeCrO_6CO_3$ and of the four reference oxides (Cr_2O_3

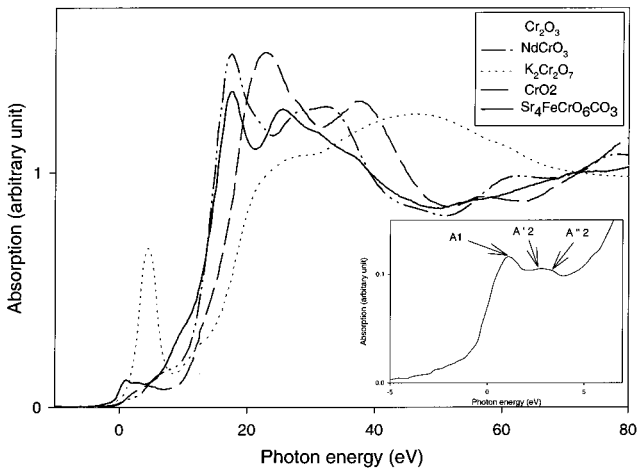

Figure 12. XANES-normalized Cr K-edges at room temperature for chromium references and $Sr_4FeCrO_6CO_3$.

Table 4. Formal Charge (FC), d_{M-O}, Energy of Main Jump Midheight (EMJM) and Equivalent Energies from Edge Integration (EE) at Cr K-edge and Fe K-edge for References and $Sr_4FeCrO_6CO_3$

compounds	FC	d_{M-O} (Å)	EMJM (eV) ± 0.3 eV	EE (eV) ± 0.3 eV
Cr_2O_3	+3	1.95 × 3 2.04 × 3	12.5	10.4
$NdCrO_3$	+3	1.97 × 4 1.98 × 2	13.9	11.4
$Sr_4FeCrO_6CO_3$	+3	1.97 × 4 1.85 × 1 2.46 × 1	13.8	10.3
CrO_2	+4	1.78 × 4 2.08 × 2	16.9	13.50
$K_2Cr_2O_7$	+6	1.54−1.71 (Cr(1)) 1.55−1.86 (Cr(2)) 1.59−1.84 (Cr(3)) 1.51−1.75 (Cr(4))	18.3 in tetrahedral configuration	
Fe_2O_3	+3	1.94 × 3 2.11 × 3	11.2	14.2
$SrFeO_{3-\delta}$	+3.7	1.92 × 4 1.98 × 2	12.1	14.9
$Sr_4FeCrO_6CO_3$	+3	1.97 × 4 1.85 × 1	11.1	14.5

and $NdCrO_3$ for Cr^{3+}, CrO_2 for Cr^{4+}, and $K_2Cr_2O_7$ for Cr^{6+} formal charges) are shown in Figure 12. The energy at midheight of the main absorption edge and the equivalent energy deduced from edge integration (Table 4) allow the oxidation state of chromium in the $Sr_4FeCrO_6CO_3$ compound to be fixed at 3+. Moreover, the small intensity of the prepeak is in agreement with an octahedral environment of chromium. The differences between Cr_2O_3, $Sr_4FeCrO_6CO_3$, and $NdCrO_3$ arise from the distortion of the oxygen octahedron around the chromium cation. The regular octahedron in $NdCrO_3$ with six similar Cr−O distances (d(Cr−O) ≈ 1.98 Å) generates a strong white line at 17.6 eV due to the occurrence of electronic transitions 1s → $4p_{x,y,z}$ at the same energy. Conversely, the octahedral distortion in $Sr_4FeCrO_6CO_3$ (or in Cr_2O_3) with three sets of Cr−O distances (d(Cr−O) ≈ 2.46, 1.97, 1.85 Å) induces a wide spread of the 1s → 4p transitions along the *x*-, *y*-, and *z*-axis, respectively. Previously, Natoli[16] developed an empirical rule linking peak energies on a XANES spectrum to the M−O distances through a simple relationship, $(E - E_0)R^2 = K$, which holds for transition metal compounds at K-edges and where E and R are the peak energy and corresponding M−O distance, whereas E_0 and K are constants to be determined for a given edge and local environment. To apply this rule to the Cr K-edge, we have determined the E_0 and K constants through precise knowledge of the Cr−O distances in two reference oxides, Cr_2O_3 and CrO_2. In $Sr_4FeCrO_6CO_3$ two distances are calculated and found equal to 1.9 and 2.4 Å, which is in good agreement with the distances calculated from neutron diffraction. The small prepeak of $Sr_4FeCrO_6CO_3$ (due to an hybridization of Cr(3d)−O(2p)−Cr(4p) orbitals) is observed (inset Figure 12) with a fine structure of two peaks A_1 and A_2 (1.10 and 2.77 eV), due to the crystal field effect on the Cr 3d orbitals: t_{2g} and e_g (separated by a gap of 1.67 eV). The latter is clearly splitted in to two small peaks A'_2 and A''_2 due to the distortion of the octahedron. The iron K-edge of $Sr_4FeCrO_6CO_3$ has been studied too (Figure 13, Table 4). The energy at midheight of the main absorption edge and the equivalent energy deduced from edge integration (Table 4) confirm the oxidation state: Fe^{3+}. The relative intensity of the prepeak due to a strong hybridization of Fe(3d)−O(2p)−Fe(4p) orbitals indicates a nonregular coordination compatible with a square pyramid.

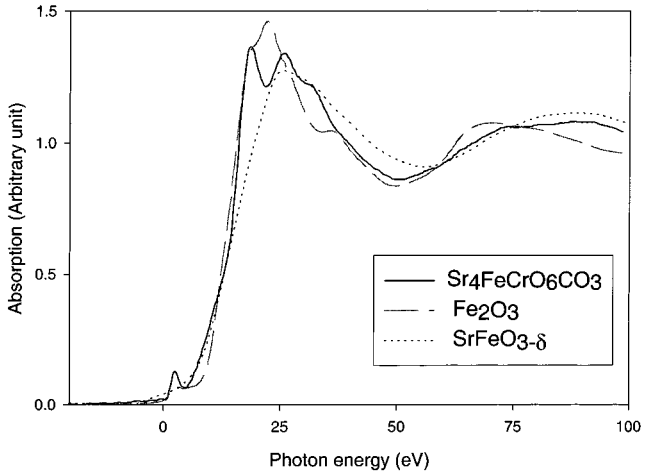

Figure 13. XANES-normalized Fe K-edges at room temperature for iron references and $Sr_4FeCrCO_3$.

Conclusion

This investigation shows for the first time the ability of chromium to accommodate carbonate goups by Cr^{3+} substitution for Fe^{3+} in $Sr_4Fe_2O_6CO_3$. The structure of $Sr_4FeCrO_6CO_3$, although closely related to $Sr_4Fe_2O_6CO_3$, differs from the latter by the transition metal polyhedra that form CrO_6 octahedra and FeO_5 pyramids distributed at random. But the great originality of the structure deals with the geometry of the carbonate layer, where CO_3 groups are connected to CrO_6 octahedra and exhibit a "coat-hanger" configuration, with four different possible orientations of the CO_3 groups. The antiferromagnetic properties of this new phase with $T_N = 125$ K, being very different from the magnetic order observed in $Sr_4Fe_2O_6CO_3$, open the route to the investigation of the magnetic properties of the $Sr_4Fe_{2-x}Cr_xO_6CO_3$ series.

CM010004I

(16) Natoli, N. In *Exafs and near edge structure*; Bianconi, A., Incoccia, L., Stipcich, S., Eds.; Springer series in thermal physics 27; Springer: New York, (Frascati, Italy, September 13−17), 1983.